Constant Power-Constant Voltage Battery Charging Based on a Loss-free Resistor Approach

D. Zambrano-Prada, A. El Aroudi, O. López-Santos, L. Vázquez-Seisdedos and L. Martínez-Salamero

***Abstract*—A constant power (CP)-constant voltage (CV) protocol for battery charging is implemented in a conventional boost converter with output filter (BOF) by imposing loss-free resistor (LFR) behavior during the CP phase. To compare on equal basis the performance of the new CP-CV technique with the classical constant current (CC)–CV protocol, the latter is also implemented in the same power stage. The CC phase in BOF is attained by imposing a G-gyrator of type II behavior to the converter. A versatile controller uses the same voltage regulation loop for both protocols during the CV phase and a slightly different loop for the CP and CC phases. The latter loop is based in both CP and CC phases on the sliding-mode control (SMC) of the input inductor current of BOF, which in steady-state is made proportional to the input voltage in the LFR case or to the output voltage in the gyrator implementation. To compensate for the slow variations of the battery voltage during the CC phase, a proportional-integral (PI) current regulator has been added in the gyrator realization. The comparison of the corresponding experimental results shows identical behavior in both approaches in the measured waveforms, component stress, efficiency and external temperature. The simplicity of the CP-CV implementation based on LFR allows the extension of the proposed protocol to other hard-switching converters.**

***Index Terms*—Battery charging, canonical elements for power processing, sliding-mode control.**

I. Introduction

THERE is a clear consensus in admitting that the main obstacles that complicate the market penetration of electric vehicles (EVs) are the so-called range anxiety (fear of not having enough charge in the vehicle), customer price, charging time and charging availability, all of them related to the battery [1]. To overcome these barriers, fast charging technique has emerged in the last years, which represents a short time of charging for both battery and energy supply system [2].

Fast charging is a multidisciplinary problem that requires a joint perception of the physical and electrochemical phenomena related to the battery technology and the electronic system interfacing a primary energy source and the battery. Charging current is often measured in terms of C, i.e., the nominal charging capacity of the battery in Ah [3], so 0.5 C or less corresponds to conventional charging while values higher or equal than C are typical of fast charging. The high currents involved in the latter case often result in energy efficiency reduction, thermal runaway, and fast degradation of characteristics, i.e., a decrease of both capacity and power of the battery.

With lithium-ion as the battery technology reference, many works reported in the last years have proposed fast charging protocols to mitigate some of the mentioned drawbacks. An interesting analysis of the mainstream papers related to those works is presented in [4] in an attempt to describe the common features of all of them. The authors in that paper point out the empirical or experimental nature of the analyzed protocols and the difficulty to extend the obtained performance to operating conditions different from the ones described in the reported experiments.

It is accepted that ten minutes fast charging could be a suitable target because it would require batteries made up of abundant and accessible raw materials at affordable cost. An experiment in that direction is the work reported in [5], in which the authors succeed in charging an energy-dense battery of 265 Wh/kg to 70% state of charge (SOC) in 11 minutes for more than 2000 cycles. 4 C charging is achieved with correct cooling and safe operation due to appropriate air convection in a thermally stable electrolyte.

Charging techniques can be classified into open-loop and closed-loop categories [6]. In the first case, there is no information fed back to the system input while in the second case the charging process is regulated dynamically. Open-loop techniques are characterized by a profile-based approach whereas closed-loop procedures are model-based allowing the formulation of an optimization problem, which is eventually solved by means of fuzzy logic or genetic algorithms. Profile-based techniques consist in a first phase of either constant current (CC), constant power (CP), multistage constant current (MCC), pulse charging, boost charging or variable current, followed in most cases by an interval of constant voltage (CV) [7]. Moreover, a comprehensive examination of model-based charging strategies can be found in [8], where it is shown that model predictive control-based algorithms are the most popular in solving the optimal charging problem although they are limited by their linear nature and their off-line implementation.

The most common charging protocol is the CC-CV, i.e. an interval of constant current followed by a phase of constant voltage. The existing alternatives take the CC-CV protocol as a reference for comparison. This is the case of the work

The D.Zambrano-Prada, A. El Aroudi, O. López-Santos and L. Martínez-Salamero are with the Group of Automatic Control and Industrial Electronics (GAEI), Rovira i Virgili University, Department of Electrical, Electronic and Automatic Control Engineering, School of Electrical and Computer Engineering, Campus Sescelades, 43007 Tarragona, Spain.

L. Vázquez-Seisdedos is with Technical University of Madrid, Department of Forestry Engineering and Management, School of Forestry Engineering and Natural Resources, Electrotechnics Teaching Unit, 28040, Madrid, Spain.

This work has been sponsored by the Spanish Ministerio de Ciencia e Innovación under grants MSCA IF EF-ST 2020/ PCI 2021-122066-2B, PID2019-111443RB-I00, and PID2020-120151RB-100.

Corresponding author: davidalejandro.zambrano@urv.cat

described in [9] where a unique CC phase is substituted by 5 CC stages, which are finally followed by a CV stage. A Taguchi method is used to obtain the optimal charging pattern for the 5-stage CC interval, which eventually results in a small improvement of the charging efficiency of around 0.6-0.9 % with respect to the CC-CV method. The trade-off between charging time and temperature rise is solved in an optimization problem in [10] by means of an off-line genetic algorithm applied to a multistage constant heating strategy, which leads to reductions of the charging time of up to almost 10% for ambient temperature of 40°C with respect to the CC-CV protocol. Another comparison with CC-CV procedure is described in [11], in which the authors use a MCC-CV strategy with adaptive features resulting from a particle swarm optimization algorithm that solves the preference of users for reducing the charging time or the battery degradation. Regarding aging loss, the proposed technique is 3.60% better than the 0.5 C CC-CV charging strategy recommended by the manufacturer.

As the previous examples reveal, the mainstream in the development of charging protocols has focused on improving the CC phase by modifying the charging characteristics or adding new stages with different current levels, in an attempt to explore exhaustively full potential of the CC techniques. Nevertheless, recent studies have considered the CP phase as a candidate for fast charging because of its energy efficiency [12] and charging speed [13], [14]. Thus, in [12] a CP-CV procedure is compared with CC-CV by simulation in a 50 kW fast charging from 20% to 90% of SOC, showing that CP-CV results in a reduction of the usable energy loss of approximately 4%. Especially relevant is the study reported in [13], where the authors evaluate the performance of lithium battery cells under five different initial charging phases: three types of CC phase, a CP phase and a proposed constant losses (CL) phase. For equal energy capacity and under the same operating conditions, the CP protocol performs similarly to the CC protocols, but improves the charge speed. This feature is further supported in [14] for the new type of Li-S battery technology, where CP charging not only improves the charge speed for a given amount of charge, but also enhances capacity retention over cycling and reduces internal losses due to the reduction of irreversible processes in the cells.

Measures reported in the above references have been obtained in a single cell with specific instrumentation for electrochemical experiments such as workstations, thermal chambers, thermostatic containers, and programmable battery test platforms among others, so they can be classified as technology related papers. Strictly speaking, the first recent overview of charging methods from a power electronics perspective is the work described in [15]. In that paper, the authors analyze battery charging methods in terms of converter topologies, power levels and control strategies. Based on the current cost of the materials, they also develop an estimation model using a genetic algorithm to forecast the optimal capacity size of a battery and the power rating of the associated on and off-board chargers. Regarding the electrical architecture of a fast charging station, the selection of the appropriate unidirectional dc-dc converter topology for the output stage has to take into account several factors such as the number of charging points, type of power distribution in the electrical architecture, and existence of galvanic isolation as described in [16]. On the other hand, the main antecedent of a battery charger operating as constant power source was reported in [17], where a half-bridge converter with an additional small inductor and two extra diodes in parallel with two dividing capacitors delivers a CP of 65 W to a 12 V lead acid battery with better thermal efficiency than both CC and CV charging. The output CP source behavior was achieved by the discontinuous voltage-mode operation of the two dividing capacitors.

In this context, it makes sense to explore the electronic implementation of some of the charging protocols by selecting an appropriate converter and control strategy, and describing the main features of the resulting experiments on a battery pack. Thus, this paper studies the implementation of a CP-CV protocol and compares its performance with that of the standard CC-CV on equal basis in the same converter. Besides charging phase duration, charge absorption, charge voltage range, absorbed energy, and other indicators such as efficiency, device stress, thermal behavior and number of components are considered in the comparison. A proof of concept is developed to charge a battery of 48 V nominal voltage from a 24 V input voltage handling a power transference of 260 W, which represents a charging process at 0.2 C. We have selected a boost converter with output filter (BOF) as a charger in order to (i) guarantee dc current without discontinuities in both ports, and (ii) develop a control strategy based on the synthesis of an appropriate canonical element for power processing. These canonical elements can be implemented by imposing their specific characteristics in steady-state by means of sliding-mode control (SMC). This strategy, expressed either in its classical formulation or in equivalent terms, is an effective solution to numerous of control problems by providing robustness under parametric uncertainties and finite-time convergence to the desired target together with a systematic design [18]–[20]. In the specific case of the CP phase, we demonstrate that a dc-dc switching converter with loss-free resistor (LFR) behavior [21] is an efficient and reliable solution to implement that charging phase. LFR behavior has been obtained by SMC applied to the input port connected in parallel with the input power supply in [22]–[24]. This type of LFR has been recently complemented with the proposal of the denominated series loss-free resistor (SLFR) [25], [26], whose virtual resistance is connected in series between the input and output port of a power stage and its power source is connected in parallel with the input voltage source.

More specifically, the main contributions of this paper are enumerated as follows:

- Implementation of a CP-CV battery charging control by imposing LFR characteristics during the CP phase in a boost converter with output filter (BOF) by means of SMC.
- Selection of the appropriate canonical element among dc transformer, G-gyrator of type I and G-gyrator of type II to impose the CC phase in the same BOF.
- Implementation of the standard CC-CV protocol by imposing Type II G-gyrator characteristics during the CC

phase in the same converter by means of SMC.
- Comparison of the CP-CV protocol with the standard CC-CV protocol in the same BOF using identical performance evaluation indicators.

The rest of the paper is organized as follows. Canonical elements for power processing are reviewed in Section II in view of their potential use as battery chargers for either CP or CC phases. The SMC design of the canonical elements in the BOF is analyzed in depth in Section III. Section IV covers exhaustively the implementation and experiments of the canonical elements selected for the mentioned phases. The insertion of a control strategy to add the CV phase to both CP and CC intervals is described in section V together with the corresponding measurements. The future extension to other converters is discussed in Section VI. Finally, conclusions and work in progress are given in Section VII.

II. Canonical Elements for Battery Charging

The standard protocol for battery charging consists of a CC charging interval (CC phase), in which the battery voltage increases up to attain a desired value v_{B_F}, followed by a CV interval (CV phase) hold until the current decreases to the vicinity of zero. An alternative protocol of the type of CP-CV is made up of a CP interval (CP phase), where the voltage increases up to attain a desired value v_{B_F} while the current decreases, followed by a CV interval. Fig. 1a. and Fig. 1b show respectively the CC-CV and CP-CV charging protocols, while Fig. 2 illustrates their corresponding power curves.

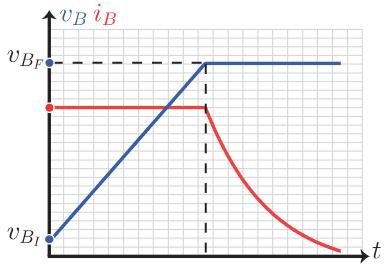

(a)

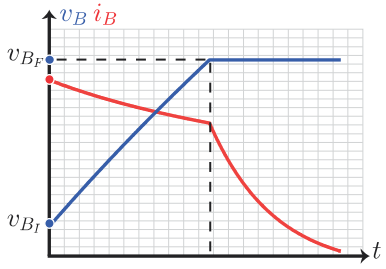

(b)

Fig. 1: Battery charging protocols (i_B=battery current; v_B=battery voltage): (a) standard CC-CV, and (b) CP-CV.

We assume in this work that the primary energy source is a regulated dc voltage V_g supplied by an appropriate internal bus of a charging station. Therefore, a non-isolated dc-dc switching converter will be the interface between the dc bus and the battery in order to perform the required charging protocol [16]. Irrespective of the function it performs, a switching converter can be modelled by any of the three canonical elements for power processing: a dc transformer [27], a power gyrator [28], and a LFR [21]. They are two-port circuits that characterize the steady-state behavior of dc-dc switching converters and are usually referred to as POPI (power output-power input) circuits because the dc input power equals the dc output power [29].

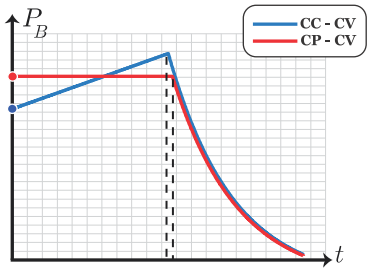

Fig. 2: Power curves of battery charging protocols.

On the other hand, what distinguishes the standard protocol from the CP-CV alternative is the first phase, which can be either performed at constant current or at constant power. Hence, it makes sense to explore the CC phase under the optics of a dc transformer or a power gyrator, and to study the CP interval with the LFR approach as illustrated in Fig. 3.

It can be observed in the transformer case that the battery current i_B in steady-state will be constant if the input current is constant and an appropriate constant value for the duty cycle D is applied, and hence the transformer ratio $n(D)$, is used. Therefore, the equations describing the dc transformer can be expressed as follows

$$v_1 = n(D)v_2 \text{ and } i_2 = \frac{i_1}{n(D)} \tag{1}$$

Similarly, using a power gyrator will yield a constant value of the battery current by imposing proportionality in steady-state between the output current and the input voltage if we choose an appropriate value of the conductance $g(D)$, and therefore of the duty cycle D. The corresponding equations of the gyrator are given by

$$i_1 = g(D)v_2 \text{ and } i_2 = g(D)v_1 \tag{2}$$

In a clear-cut contrast, the LFR feeds the battery with the constant power absorbed by the emulated resistor r at its input port and is characterized by the following equations.

$$i_1 = \frac{v_1}{r} \text{ and } v_2 i_2 = r i_1^2 \tag{3}$$

In order to compare on equal basis the performance of CC and CP phases, the same converter will be used. A conventional boost converter is apparently a good candidate for the LFR approach since it results in a single stable equilibrium point (EP) with LFR behavior when loaded with a generic nonlinear static load (GNSL) that can be particularized as a battery as explained in [30]. However, the output current is discontinuous, which introduces an undesired ripple in

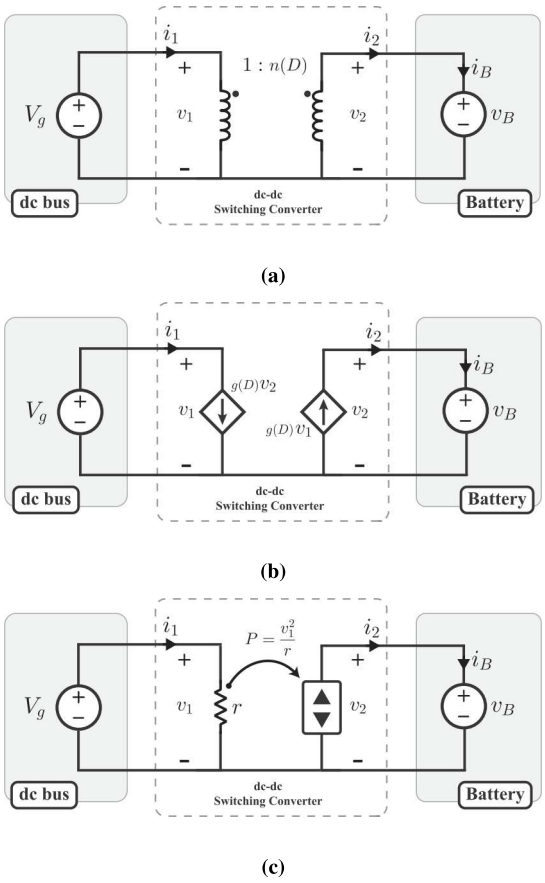

Fig. 3: Modelling the first phase of battery charging by means of canonical elements. (a) dc transformer, (b) power gyrator and (c) LFR.

the battery and precludes its control in sliding-mode. This drawback has led to include an output filter, and therefore to consider a BOF as the power converter in which both CC-CV and CP-CV protocols can be theoretically studied and experimentally verified.

III. SMC-BASED DESIGN OF CANONICAL ELEMENTS

Fig. 4 shows the block diagram of a sliding-mode controlled BOF unidirectional battery charger. Controlled switch Q_1 and diode D_1 are assumed ideal and no parasitic elements are considered. Losses on the passive components are neglected. For the sake of the subsequent experimental implementation, a general sliding surface made up of a linear combination of both input and output ports variables is represented in the figure.

It is worth mentioning that capacitor C_2 is optional since its filtering effects can be accomplished by the internal capacity of the battery. For that reason, C_2 will not be considered in our analysis and hence the battery charging current will be i_2. Therefore, the expression of the switching function $S(x)$ will be given by

$$S(x) = \alpha V_g + \beta i_1 + \gamma v_B + \delta i_2 \tag{4}$$

It can be observed that particularizing expression (4) for certain parameter values might result in: (i) a dc transformer

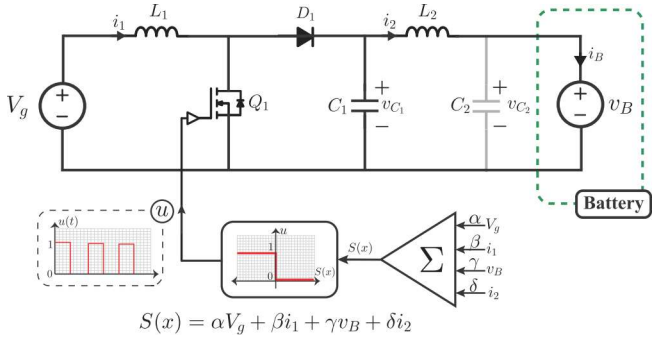

Fig. 4: Block diagram of a sliding-mode controlled BOF unidirectional battery charger.

[31], (ii) a power G-gyrator of type I [32]. (iii) a power G-gyrator of type II [33], and (iv) a LFR [22]. The four cases and the corresponding parameter constraints are summarized in Table I.

TABLE I: Particularizing the sliding variable $S(x)$ for different canonical elements.

Parameter constraint	Sliding surface	Canonical element
$\alpha = \gamma = 0$	$S(x) = \beta i_1 + \delta i_2$	dc transformer
$\beta = \gamma = 0$	$S(x) = \alpha V_g + \delta i_2$	G-gyrator type I
$\alpha = \delta = 0$	$S(x) = \beta i_1 + \gamma v_B$	G-gyrator type II
$\gamma = \delta = 0$	$S(x) = \alpha V_g + \beta i_1$	LFR

The control law to keep the state trajectory switching above and below surface $\Sigma = \{x | S(x) = 0\}$ is derived from the conditions for existence of sliding motions on this surface [34]. These are:

$$\frac{dS(x)}{dt} < 0 \quad \text{if} \quad S(x) > 0 \tag{5a}$$

$$\frac{dS(x)}{dt} > 0 \quad \text{if} \quad S(x) < 0 \tag{5b}$$

The above conditions are fulfilled when the switching law is given by

$$u = \begin{cases} 0, & \text{if, } S(x) > 0 \\ 1, & \text{if, } S(x) < 0 \end{cases} \tag{6}$$

A. State equations

In continuous conduction mode (CCM), the converter in Fig. 4 can be described in compact form by the following set of differential equations

$$\frac{di_1}{dt} = \frac{V_g}{L_1} - \frac{v_{C_1}}{L_1}(1-u) \tag{7a}$$

$$\frac{di_2}{dt} = \frac{v_{C_1}}{L_2} - \frac{v_B}{L_2} \tag{7b}$$

$$\frac{dv_{C_1}}{dt} = \frac{i_1}{C_1}(1-u) - \frac{i_2}{C_1} \tag{7c}$$

In equations (7), i_1 is the input inductor current, i_2 is the output inductor current, v_{C1} is the capacitor voltage and u is a binary control signal to activate/deactivate the controlled switch Q_1, so that $u = 1$ corresponds to the ON state and $u = 0$ corresponds to the OFF state.

B. Existence of sliding-mode

Assuming a constant input voltage V_g, the time-derivative of the sliding variable $S(x)$ can be expressed as follows:

$$\dot{S}(x) \triangleq \frac{dS(x)}{dt} = \beta\frac{di_1}{dt} + \gamma\frac{dv_B}{dt} + \delta\frac{di_2}{dt} \tag{8}$$

Taking into account (5) in (8) and the switching policy given by expression (6), we study next the existence of sliding-mode in the four cases illustrated in Table I.

1) dc transformer: The constraint $\gamma = 0$ in (8) yields

$$\frac{dS(x)}{dt} = \beta\frac{di_1}{dt} + \delta\frac{di_2}{dt} \tag{9}$$

On the other hand, $S(x) < 0$ implies $u = 1$ and therefore expression (9) becomes

$$\frac{dS(x)}{dt} = \beta\frac{V_g}{L_1} + \delta\frac{(v_{C_1} - v_B)}{L_2} \tag{10}$$

In steady-state $v_{C_1} = v_B$, which implies

$$\frac{dS(x)}{dt} = \beta\frac{V_g}{L_1} > 0, \quad \forall\beta > 0 \tag{11}$$

Similarly, $S(x) > 0$ implies $u = 0$, and hence expression (9) results in

$$\frac{dS(x)}{dt} = \beta\frac{(V_g - v_{C_1})}{L_1} + \delta\frac{(v_{C_1} - v_B)}{L_2} \tag{12}$$

In steady-state, $v_{C_1} = v_B$ and $V_g < v_{C_1}$, which yields

$$\frac{dS(x)}{dt} = \beta\frac{(V_g - v_{C_1})}{L_1} < 0 \tag{13}$$

Therefore, the control law given by expression (6) induces sliding motions in a dc transformer based on BOF.

2) G-gyrator of type I: The constraints in the parameters are $\beta = \gamma = 0$, which results in

$$\frac{dS(x)}{dt} = \delta\frac{di_2}{dt} = \delta\frac{(v_{C_1} - v_B)}{L_2} \tag{14}$$

Since expression (14) does not depend on the control variable u and, in addition, is zero in steady-state, sliding-mode will not exist in this case.

3) G-gyrator of type II: In this case, the constraint $\delta = 0$ in (8) results in

$$\frac{dS(x)}{dt} = \beta\frac{di_1}{dt} + \gamma\frac{dv_B}{dt} \tag{15}$$

Therefore, $S(x) < 0$ and $u = 1$ leads to

$$\frac{dS(x)}{dt} = \beta\frac{V_g}{L_1} + \gamma\frac{dv_B}{dt} \tag{16}$$

where the second term is greater than zero because $v_B(t)$ is a growing function of time during the charging process.

Assuming $\beta > 0$, expression (16) will be positive if the following condition is fulfilled

$$\beta\frac{V_g}{L_1} > |\gamma|\frac{dv_B}{dt} \tag{17}$$

For $S(x) > 0$ and $u = 0$, expression (15) becomes

$$\frac{dS(x)}{dt} = \beta\frac{V_g - v_{C_1}}{L_1} + \gamma\frac{dv_B}{dt} \tag{18}$$

Given that $V_g - v_{C_1} < 0$ in steady-state, expression (18) will be negative if $\gamma < 0$. Since expression (16) can be positive and expression (18) negative with an appropriate selection of β and γ, it can be concluded that the control law (6) will lead to a sliding behavior in a G-gyrator of type II based on BOF.

4) Loss-free resistor: Introducing $\gamma = \delta = 0$ in (8) results in

$$\frac{dS(x)}{dt} = \beta\frac{di_1}{dt} \tag{19}$$

Hence, for $S(x) < 0$ and $u = 1$, expression (19) becomes

$$\frac{dS_6(x)}{dt} = \beta\frac{\beta V_g}{L_1} > 0, \quad \forall\beta > 0 \tag{20}$$

which is again inequality (11). Also, for $S(x) > 0$ and $u = 0$, we obtain inequality (13). Therefore, the control given by expression (6) will generate sliding motions in BOF-based LFR.

C. Equivalent control and ideal sliding dynamics

In sliding-mode, the converter dynamics is subjected to the constraints $S(x) = 0$ and $\dot{S}(x) = 0$. Therefore, equaling (8) to zero leads to the following general expression of the equivalent control u_{eq}:

$$u_{eq} = 1 - \frac{V_g + \frac{L_1\delta}{L_2\beta}(v_{C_1} - v_B) + \frac{L_1\gamma}{\beta}\frac{dv_B}{dt}}{v_{C_1}} \tag{21}$$

Replacing the switched binary signal u by the expression of the equivalent control (21) in the converter state equations given by (7) and imposing the different constraints of Table I will yield the ideal sliding dynamics for dc transformer, G-gyrator of type II, and LFR.

1) dc transformer: In this case $S(x) = 0$ implies $i_2 = -(\beta/\delta)i_1$, and $\gamma = 0$ leads to

$$u_{eq} = 1 - \frac{V_g + \frac{L_1\delta}{L_2\beta}(v_{C_1} - v_B)}{v_{C_1}} \tag{22}$$

Hence, the ideal sliding dynamics will be given by

$$\frac{di_1}{dt} = -\frac{\delta(v_{C_1} - v_B)}{\beta L_2} \tag{23a}$$

$$\frac{dv_{C_1}}{dt} = \frac{i_1\left(V_g + \frac{L_1\delta}{L_2\beta}(v_{C_1} - v_B)\right)}{C_1 v_{C_1}} + \frac{\beta i_1}{C_1\delta} \tag{23b}$$

2) G-gyrator of type II: In sliding-mode $S(x) = 0$, which implies for this type of gyrator $i_1 = -(\gamma/\beta)v_B$. On the other hand, $\delta = 0$ leads to the following expression of the equivalent control:

$$u_{eq} = 1 \; - \; \frac{V_g \; + \frac{L_1\gamma}{\beta}\frac{dv_B}{dt}}{v_{C_1}} \tag{24}$$

Consequently, the ideal sliding dynamics can be expressed as follows

$$\frac{di_2}{dt} \;\; = \;\; -\frac{v_{C_1} - v_B}{L_2} \tag{25a}$$

$$\frac{dv_{C_1}}{dt} \;\; = \;\; -\frac{\gamma v_B}{\beta}\left(\frac{V_g + \frac{L_1\gamma}{\beta}\frac{dv_B}{dt}}{C_1 v_{C_1}}\right) - \frac{i_2}{C_1} \tag{25b}$$

3) Loss-free resistor: In the LFR behavior, the sliding-mode will be characterized by $i_1 = -(\alpha/\beta)V_g$. Besides, the constraints $\delta = \gamma = 0$ yield the following expression of the equivalent control.

$$u_{eq} = 1 \; - \frac{V_g}{v_{C_1}} \tag{26}$$

Consequently, the ideal sliding dynamics can be expressed as follows

$$\frac{di_2}{dt} = \; -\frac{(v_{C_1} - v_B)}{L_2} \tag{27a}$$

$$\frac{dv_{C_1}}{dt} = -\frac{\alpha V_g^2}{\beta C_1 v_{C_1}} \; - \frac{i_2}{C_1} \tag{27b}$$

D. Equilibrium points

By equaling to zero equations (23), (25) and (27), the expressions of EP in the dc transformer, G-gyrator of type II, and LFR cases is obtained. As it could be expected, the value of the capacitor voltage v_{C_1} in equilibrium is equal to that of the battery voltage in the three cases, i.e., $V_{C_1}^* = V_B^*$, where the asterisk and capital letters stand the EP.

In all three cases, the nature of POPI circuit is verified at EP while the particular features of each case are the following

$$I_2^* = -\frac{\beta}{\delta}I_1^*, \quad \text{dc transformer} \tag{28a}$$

$$I_1^* = -\frac{\gamma}{\beta}V_B^*, \quad \text{G-gyrator of type II} \tag{28b}$$

$$I_1^* = -\frac{\alpha}{\beta}V_g, \quad \text{LFR} \tag{28c}$$

E. Stability conditions

Linearizing equations (23), (25) and (27) in the vicinity of their corresponding EP results in the characteristic equation $s^2 + bs + c = 0$, whose coefficients b and c are shown in Table II for each canonical element together with the conditions to ensure both stability and the existence of sliding-mode. Note that the dc transformer is marginally stable and, for that reason, it will be excluded in the synthesis of the CC phase based on BOF. See Appendix A for the detailed stability analysis.

IV. G-GYRATOR OF TYPE II-BASED CC VS LFR-BASED CP CHARGING: IMPLEMENTATION AND EXPERIMENTS

The analysis in the previous section has shown that the best solution for CC charging in BOF is imposing a type II G-gyrator behavior in the converter because it requires simple design conditions for both sliding-mode existence and subsequent stability. Similarly, it has been demonstrated in the same section that the CP alternative can be easily implemented with the LFR approach.

For the previous reasons, we have implemented both charging protocols in the experimental setup shown in Fig. 5a. It can be observed in the picture the input voltage source, BOF stage and control circuitry in Fig. 5b, and battery pack with its battery management system (BMS) in Fig. 5c.

Fig. 6 illustrates the circuitry corresponding to the power stage and Fig. 7a and Fig. 7b show the controller, which is has versatile structure with a common part for both CC and CP phases and a specific part for each of them.

Inductors L_1 and L_2 have been built from Magnetics Kool Mu cores ref. 77995 with values of 60 μH and 100 μH, and maximum dc currents of 20 A and 10 A, respectively. The input inductor L_1 have been designed in order to operate at 100 kHz with a ripple current of 1.25 A. The output capacitor of 47 μF and inductor L_2 constitute a low-pass filter for the output current with a cut-off frequency of 10 kHz. The capacitors in input and output ports with capacitance 100 μF and 20 μF respectively are added to provide filtering in each port. The power stage uses a dual diode VX60M100PWHM3 to implement diode D_1 in Fig. 4 and an auxiliary diode connecting the input voltage to the intermediate voltage v_{C1} during start-up to mitigate the effect of the inrush current. Controlled switch Q_1 in Fig. 4 has been implemented by a MOSFET STW56N60M2, which is activated by the isolated driver TLP 350H. Current i_1 is measured by sensor LA 25-NP while input and output voltages are both sensed by LV 25-P. The power generator SM 70-45 D has been used as input voltage source while the output load is a battery pack of 20 cells of lithium-titanate-oxide (LTO) ELERIX EX-T30K resulting in a nominal voltage of 48 V. Finally, the charging process supervision indicated in Fig. 5c is carried out by 123ELECTRIC BMS123 Smart.

The practical implementation of the sliding–mode control requires a hysteresis modulator to establish a finite value of the switching frequency in the range of safe operation of the power semiconductors. Then, expression (6) is modified as follows

$$u = \begin{cases} 0, & \text{if, } S(x) > +\Delta \\ 1, & \text{if, } S(x) < -\Delta \end{cases} \tag{29}$$

where Δ is a suitable hysteresis width for tuning the switching frequency at a desired value.

Fig. 7a depicts the hysteresis modulator that has been used in the controller implementation. The value of Δ is introduced

TABLE II: Conditions for stability and sliding-mode existence for each canonical element based on BOF.

Canonical element	b	c	Stability	sliding-mode
dc transformer	$\frac{I_2^*}{C_1 V_{C_1}^*}\left(1+\frac{L_1\delta^2}{L_2\beta^2}\right)$	0	Marginal	$\beta>0$
G-gyrator of type II	$-\frac{\gamma V_g}{\beta C_1 V_{C_1}^*}$	$\frac{1}{L_2C_1}$	$\beta>0$	$\beta>0$
				$\gamma<0$
			$\gamma<0$	$\frac{\beta V_g}{L_1}+\gamma\frac{dv_B}{dt}>0$
Loss-free resistor	$-\frac{\alpha V_g^2}{\beta C_1 {V_{C_1}^*}^2}$	$\frac{1}{L_2C_1}$	$\beta>0$	$\beta>0$
			$\alpha<0$	

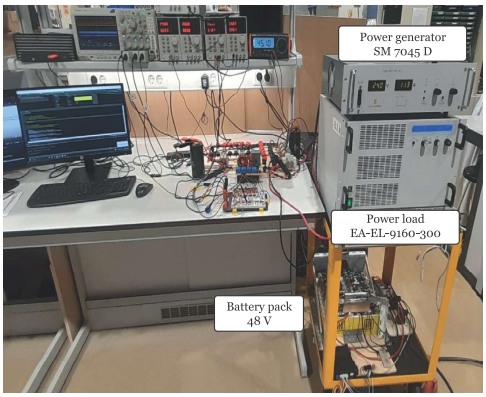

(a)

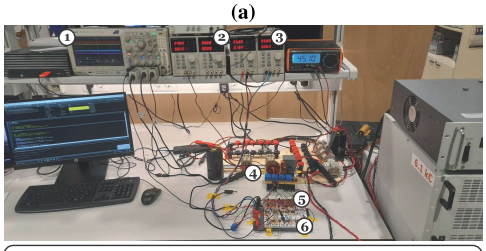

(b)

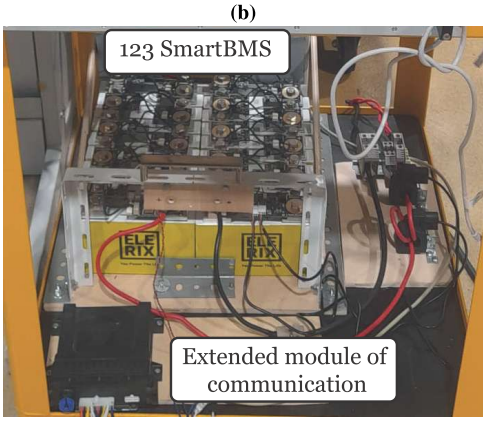

(c)

Fig. 5: Experimental setup for CC and CP charging: (a) Complete. (b) Control. (c) BMS of battery pack.

by the input potentiometer and transformed into the opposite value $-\Delta$ by means of an operational amplifier-based inverter stage. With Δ and $-\Delta$, a hysteresis comparator whose input is the switching function $S(x)$ has been implemented. This stage is then followed by a J-K flip-flop to adapt the output of the comparator to the activation/ deactivation levels required by the transistor driver TLP350H.

On the other hand, the specific value of the switching function $S(x)$ for CC or CP can be obtained in the circuit of Fig. 7b by selecting the options g_{gyr} or g_{LFR} in the input potentiometer and the respective values of v_B and V_g in the input of the analog multiplier AD633. Thus, the sliding functions $S_1(x)=i_1-g_{\text{gyr}}v_B$ for the type II G-gyrator, with $g_{\text{gyr}}=-\gamma/\beta>0$, and $S_2(x)=i_1-g_{\text{LFR}}V_g$ for the LFR, with $g_{\text{LFR}}=-\alpha/\beta>0$, can be selected.

A. CP charging results

The output battery has been charged from an initial voltage of 42 V to a final value of 48 V with a constant power of 260 W using an input voltage of 24 V and $g_{\text{LFR}}=470$ mS. Fig. 8 shows the measured waveforms of the BOF start-up in the CP phase. Input voltage V_g, output current i_2, and battery voltage v_B are represented in a 1:1 scale while current i_1 is displayed in a reduced 1:1/2 scale. It can be observed the expected constant behavior of currents i_1 and i_2 after a settling time of 6.4 ms of the input voltage.

The steady-state behavior of the waveforms of Fig. 8 is represented in detail in Figs. 9a-9c for different values of the battery voltage during the charging process. Namely, initial value of 42 V, intermediate value of 45 V, and final value of 48 V. The waveform corresponding to the output constant power of 260 W used for the CP charging has been added. It can be observed in the bottom of the figures that the mean values of input voltage and input current remain unaltered in the three cases ensuring the constant power supply while the mean value of the output current changes in an inverse proportion to the value of the battery voltage as it can be expected in the CP phase.

B. CC Charging Results

In the CC phase, the output battery has been also charged from an initial voltage of 42 V to a final value of 48 V with a constant current of 6 A using an input voltage of 24 V.

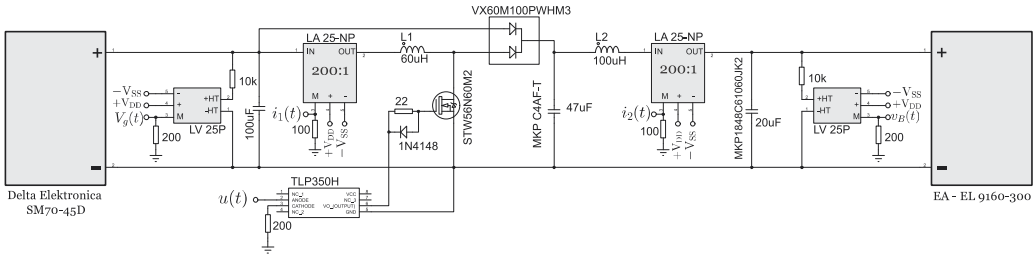

Fig. 6: Circuit scheme of the BOF stage.

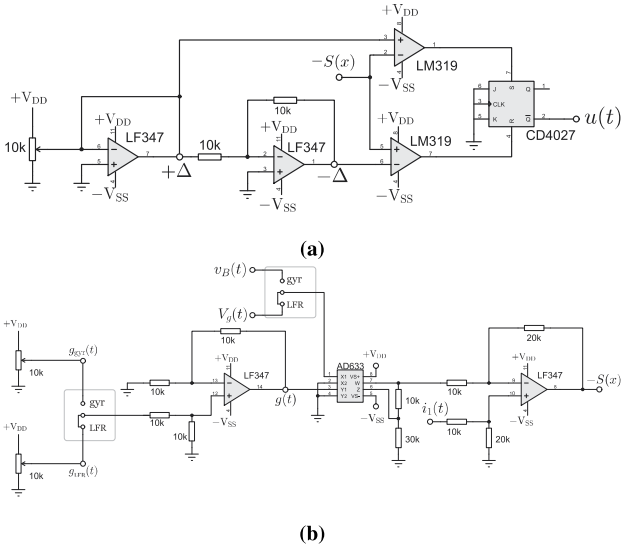

Fig. 7: Circuit scheme of the controller for CC or CP charging in BOF: (a) Hysteresis modulator. (b) Switching surface for CC or CP.

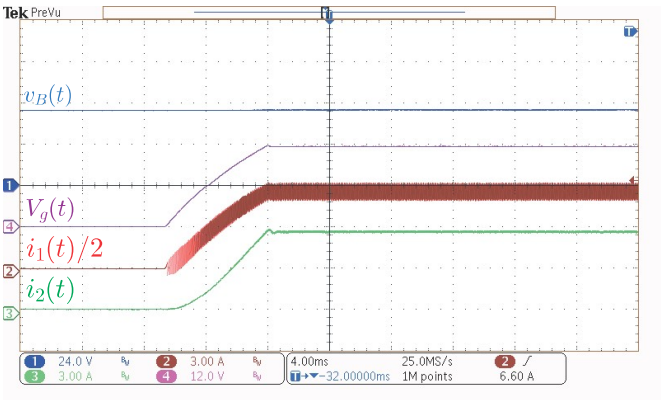

Fig. 8: Input voltage, input current, output current and battery voltage during of the BOF start-up in CP phase.

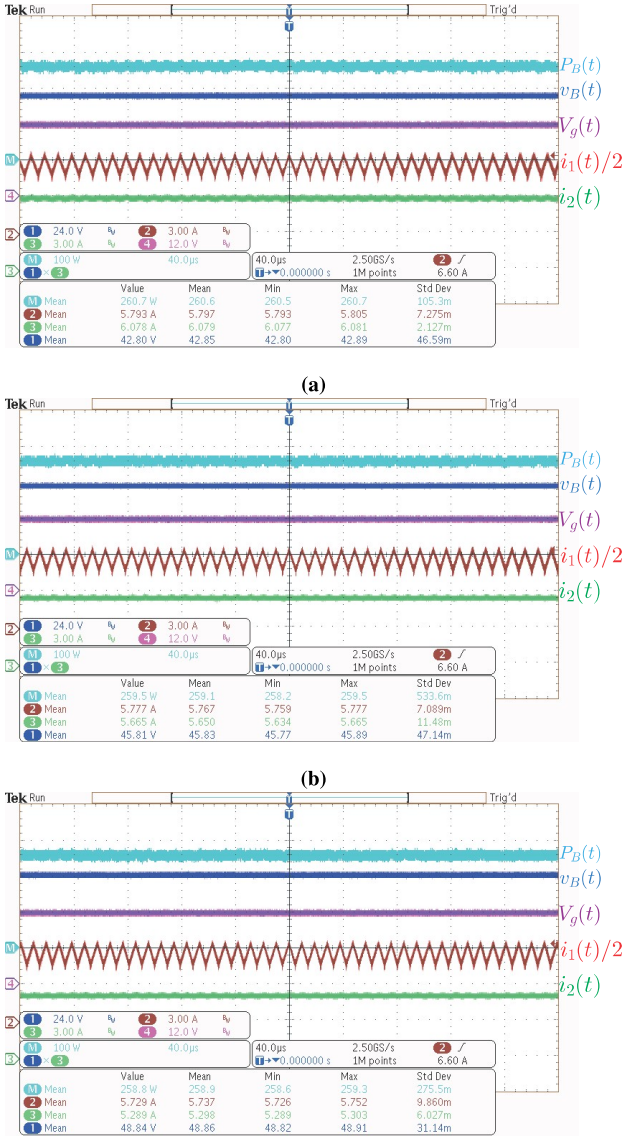

Fig. 9: Steady state waveforms of output power, battery voltage, input voltage, input current, and output current of the BOF during CP phase. (a) Battery voltage of 42 V. (b) Battery voltage of 45 V. (c) Battery voltage of 48 V.

The output current is kept constant by the insertion of a PI controller in the implementation of the conductance g_{gyr} loop. Otherwise, the input current would change slowly following the variations of the battery voltage and therefore the output current would also change in a similar way.

Fig. 10 shows the measured waveforms of the BOF during start-up in the CC phase. Input voltage V_g, output current i_2, and battery voltage v_B are represented in a 1:1 scale while current i_1 is displayed in a reduced 1:1/2 scale. It can be observed the expected constant behavior of currents i_1 and i_2 after a settling time of 10 ms of the input voltage.

The steady-state behavior of the waveforms of Fig. 10 is represented in detail in Figs. 11a-11c for different values of the battery voltage during the charging process. Namely, initial

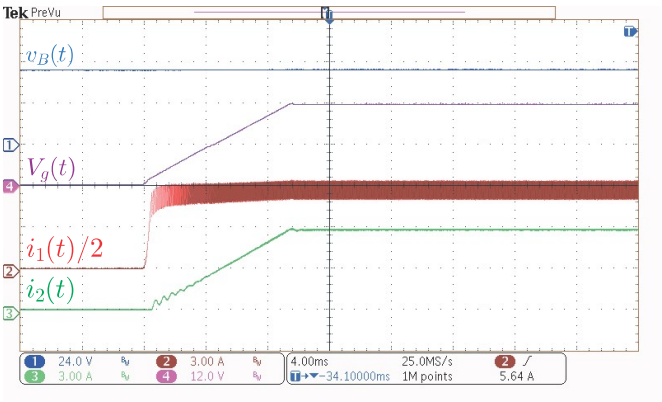

Fig. 10: Input voltage, input current, output current and battery voltage during BOF start-up in CC phase.

value of 42 V, intermediate value of 45 V, and final value of 48 V. The waveform corresponding to the output power that results in the CC charging has been added. It can be observed in the bottom of the figures that the mean value of the output current remains practically unaltered in the three cases ensuring the constant current supply while the mean value of the output power changes proportionally to the value of the battery voltage as it can be expected in the CC phase.

C. Comparative Analysis Between CP and CC Phases

The first conclusion in the measured waveform comparison of the CP and CC phases is that both approaches are equivalent, which includes in practice an identical stress of the power devices and similar efficiency ranging from 94 % to 96 %. This is due to the fact that the respective switching functions of CP and CC are linear combinations involving the input inductor current, which implies similar behavior of the system in ON and OFF states. In the particular case of the BOF, the implementation of the gyrator requires the insertion of a PI control loop to compensate the variation of the battery voltage during the charging process and ensure a constant value of the output current. Apart from this small extra number of components in CC, no significant differences are observed.

The equivalence between both phases reaches the thermal behavior of the BOF as illustrated in Fig. 12. In Fig. 12a the part of the power stage used for temperature measurements is depicted and in Figs. 12b and 12c, the thermography corresponding to CP (LFR) and CC (gyrator), respectively is shown. The experiments have been carried out using an electronic load EA-EL-9160-300 with an output voltage of 45 V to emulate the battery, which has led to similar waveforms to the ones shown in Figs. 9 and 11.

V. Complete Charging Protocol For Both Approaches

The CV phase is characterized by the regulation of the battery voltage at specified level v_{Bf} that has been previously reached in either CC or CP phases. The versatility of the design in Fig. 7 for phases CC and CP is extended now for a complete charging protocol as illustrated in the block diagram of Fig. 13.

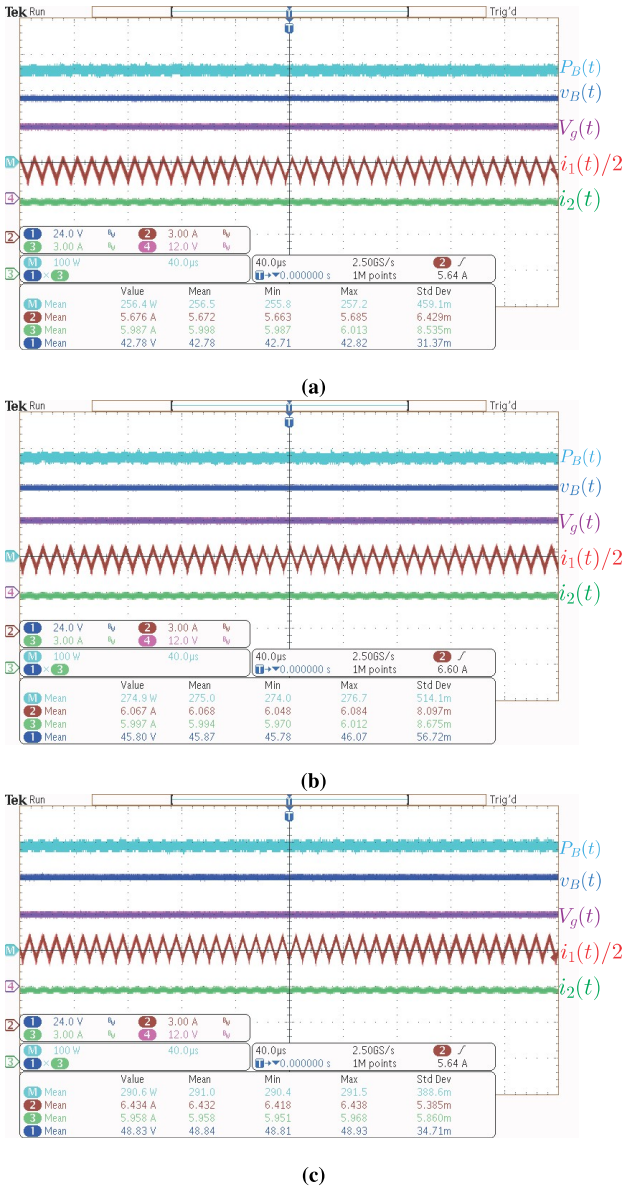

Fig. 11: Steady state waveforms of output power, battery voltage, input voltage, input current, and output current in BOF during CC phase. (a) Battery voltage of 42 V. (b) Battery voltage of 45 V. (c) Battery voltage of 48 V.

In the diagram, conductance $g_1(t)$ characterizes the current loop and can represent equally g_{gyr} or g_{LFR}. Note that the actual value of the conductance in the gyrator case is obtained at the output of transfer function C_{i_2} to compensate the variations of the output current produced by the increase of the battery voltage during the charging process. Conductance $g_2(t)$, in turn, is the output of the voltage loop that regulates the battery voltage. During CC or CP phases, the binary variable `mode` in the figure disables the voltage regulation loop, so $g_2(t)$ is zero and the effective conductance $g(t)$ is $g_1(t)$. When the battery voltage reaches the specified level v_{Bf}, the variable `mode` enables the voltage regulation loop and disables the current loop, so the effective conductance $g(t)$ is $g_2(t)$.

With this aim, the circuit input of Fig. 7b has been modified by including $g_2(t)$ as illustrated in Fig. 14a. Conductance $g_2(t)$

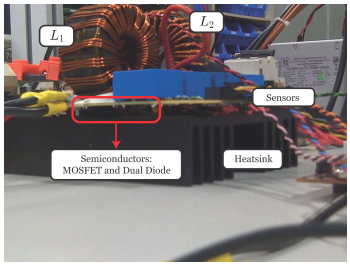

(a)

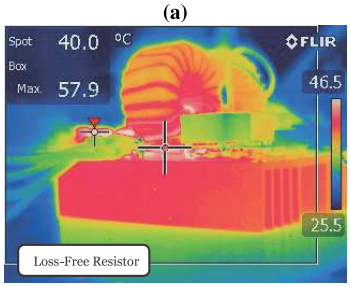

(b)

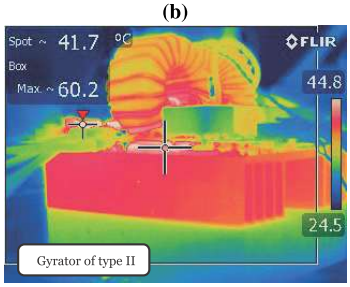

(c)

Fig. 12: Thermal behavior in BOF during CP and CC phases. (a) Measured part of the power stage. (b) CP termography. (c) CC termography.

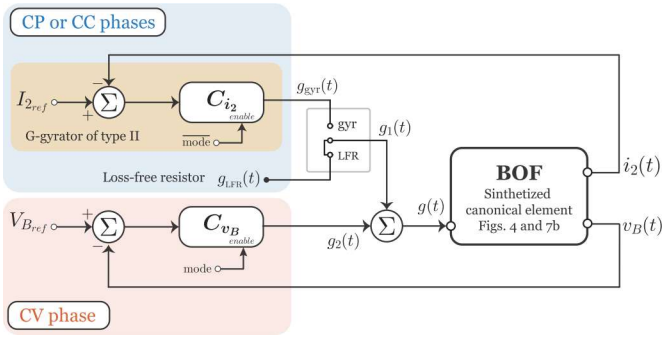

Fig. 13: Block diagram of the control system for the complete charging protocol in BOF for either CP-CV or CC-CV.

is obtained as shown in Fig. 14b where the binary variable `mode` yields a value of $g_2(t)$ equal to a linear combination of the output voltage error and its integral when `mode` $= 1$ and to a zero value of $g_2(t)$ when `mode` $= 1$. Finally Fig. 14c shows the generation of $g_1(t)$ in the gyrator case, which includes a PI compensating network in the second operational amplifier-based stage that implements the transfer function C_{i_2}.

Figs. 15 and 16 show respectively the complete charging process of the battery for the CP-CV and CC-CV approaches, respectively. In the first case, the initial value of the battery

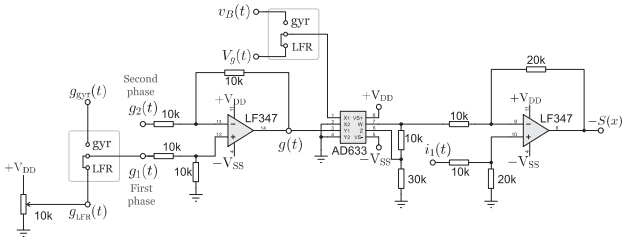

(a)

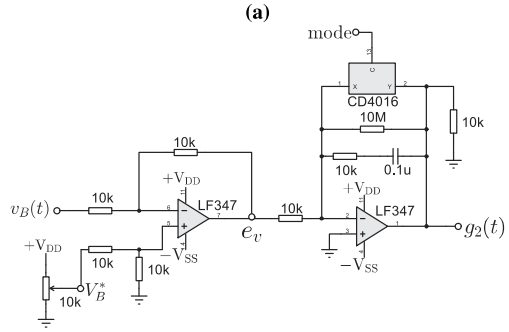

(b)

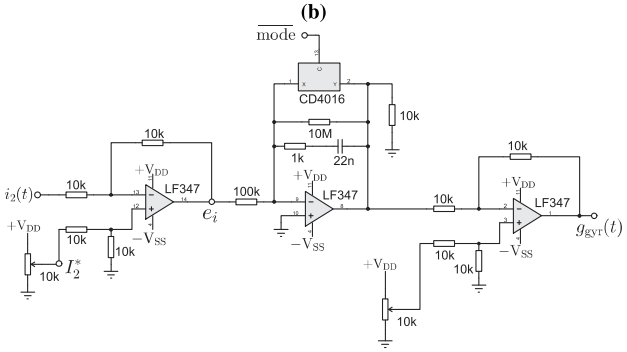

(c)

Fig. 14: Circuit schematic diagram of the controller for the complete charging protocol in BOF for either CP-CV or CC-CV. (a) Switching function. (b) Generation of $g_2(t)$. (c) Generation of $g_1(t)$ in the gyrator case.

voltage is 44.09 V and a final value of 47.9 V is reached with a constant charging power of 260 W $\pm$ 1 W. In the CC-CV protocol, the respective initial and final voltages are 44.27 V and 48 V for a constant charging current of 6 A. In both charging processes, the maximum output current has been set to 6 A, and the transition for CV phase occurs when the battery voltage reaches a value of 47.3 V. The complete charging time has taken 3 hours for the CP-CV and 2.5 hours for the CC-CV.

TABLE III: Comparison between CP phase and CC phase.

Charging phase	Duration phase [s]	Absorbed charge [kC]	Voltage range [V]	Absorbed energy per time [Ws]
CP	7298	41.79	3.21	18.4029
CC	6401	35.09	3.03	17.6106

Table III relates only the CP and CC phases of Figs. 15 and 16 in terms of duration, charge absorbed (calculated by

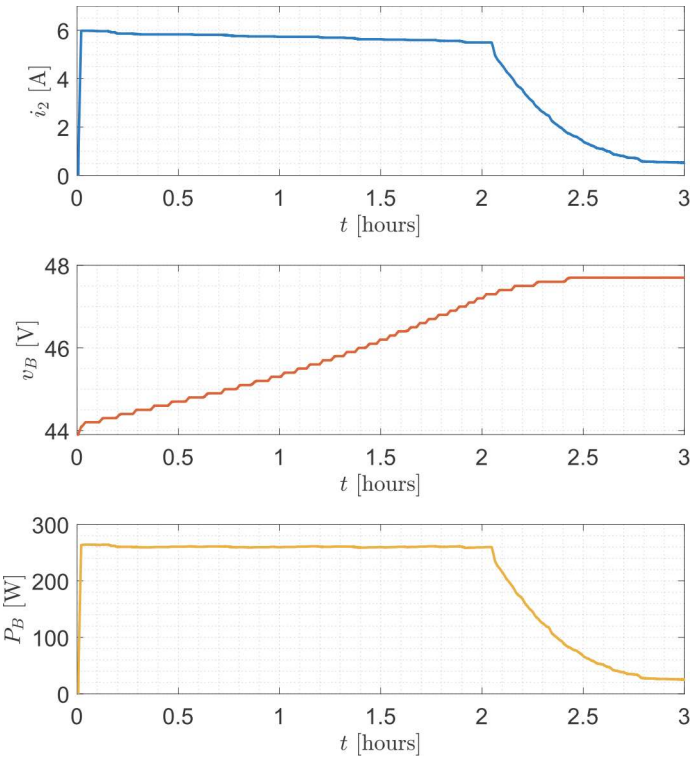

Fig. 15: Experimental waveforms in the CP-CV charging protocol. From top to bottom: output current, battery voltage and output power.

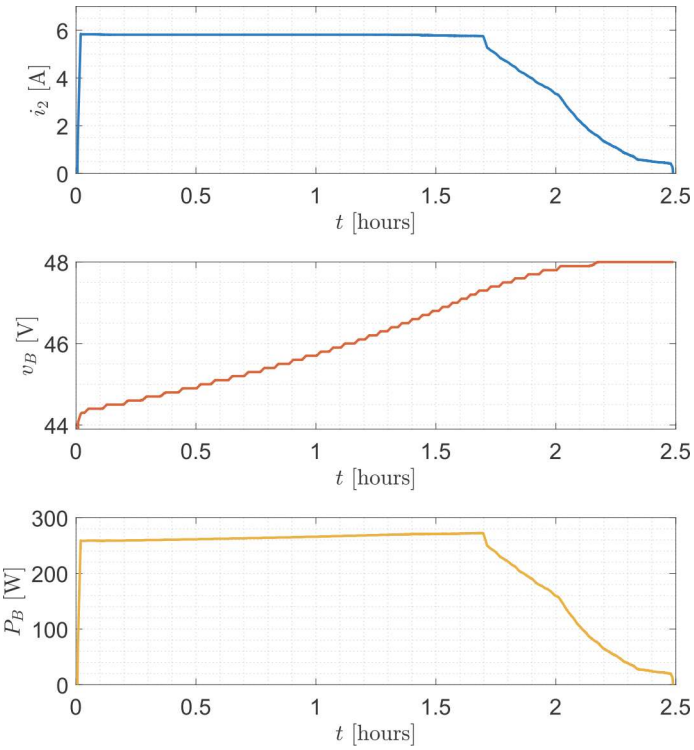

Fig. 16: Experimental waveforms in the CC-CV charging protocol. From top to bottom: output current, battery voltage and output power.

coulomb counting method $\int i_B dt$), and energy absorbed in the voltage range from the start of the charging process until the transition to the CV stage (calculated by multiplying the charge and Δv_B during the phase). The experimental data show that the CP phase supplies the battery with 4.5% more charge than the CC phase, despite the fact that the output current of BOF in CP phase reaches a maximum of 6 A at the beginning and then decreases.

VI. Extension to Other Converters

It has been demonstrated in the previous section that the CP-CV protocol can compete with the classical CC-CV technique, and that can be easily implemented in hard switching converters using the LFR-approach. In order to facilitate the comparison of both protocols operating on the same power stage, the demonstration has been centered in a BOF circuit, which is a voltage step-up converter. A dual case for equal basis comparison could also be envisaged in a buck converter with input filter (Fig. 17) for voltage step-down applications. In such case, the control for g_{gyr} or g_{LFR} implementation must circumvent the unstable behavior that arises in both gyrator [32] and LFR [22] realizations.

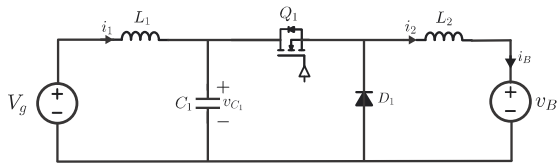

Fig. 17: Buck converter with input filter (BIF).

Regarding the implementation of the CP-CV protocol equally for voltage step-up or step-down applications, SEPIC and Cuk converters can be used in either their isolated or non-isolated versions depicted in Fig. 18 since they can lead to stable LFR behavior as demonstrated in [22]. Note that the use of the non-isolated version of these converters could also extend the CP-CV application to a non-isolated bus with regulated voltage V_g.

On the other hand, the battery used in the experiments has a nominal capacity C of 30 Ah and has been charged at 0.2 C in CC-CV protocol and corresponding equivalent power of 260 W in CP-CV protocol, which represents a conventional charging. The extension to ultrafast charging will imply in this case attaining 1.5 C by increasing the effective charging current or charging power, which could be performed by the paralleling of three BOF stages as illustrated in Fig. 19, each stage operating at 0.5 C. In this context, redesigning the system for constant switching frequency would allow the interleaved operation of the BOF converters and result in a reduction of the size of the passive elements [35].

VII. Conclusion

It has been shown that a dc-dc switching converter with loss-free resistor (LFR) behavior is an efficient and reliable solution to implement a CP-CV battery charging protocol offering enhanced performance in terms of amount of charge per unit of time when it is compared with the conventional CC-CV procedure in the same power conversion stage and battery pack. A comparison between both protocols have been carried out in a BOF that allows implementing the respective phases CP and CC by means of sliding-mode control applied to

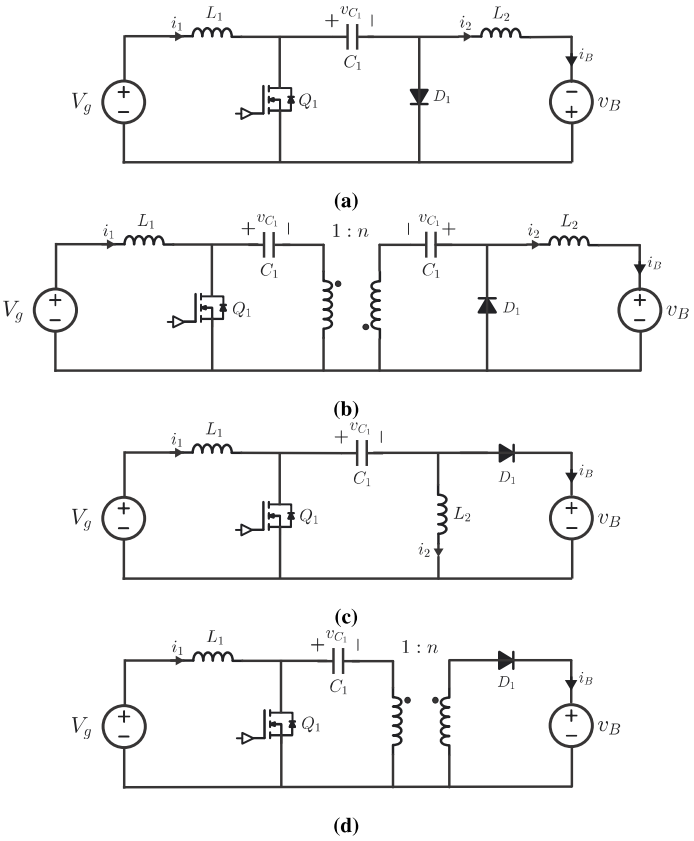

Fig. 18: Candidates for CP-CV protocol based on LFR for voltage step-up and step-down applications. (a) Non-isolated Ćuk converter. (b) Isolated Ćuk converter. (c) Non-isolated SEPIC converter. (d) SEPIC converter.

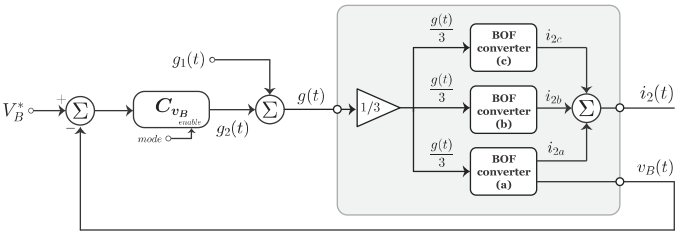

Fig. 19: Block diagram of the parallel connection of 3 BOFs with democratic current sharing.

the input inductor current. The resulting control imposes LFR behavior for the CP phase, and type II-gyrator characteristics for the CC interval.

The implemented controller uses the same voltage regulation loop for both protocols and similar circuitry for CP and CC regulation loops. The main difference being the insertion of a PI network in the gyrator implementation to compensate the slow variations of the battery voltage during the first phase of the charging process.

Although the BOF characteristics imply a voltage step-up application, the procedure can be extended to voltage step-down cases where the buck converter with input filter represents the dual problem. In this context, it is apparent that an optimal converter for CP-CV protocol based on LFR could be the SEPIC or the isolated version of the Ćuk converter since they provide equally voltage step-down and step-up characteristics together with galvanic isolation between the input bus voltage and the battery.

The experiments have been carried for normal charging at 0.2 C to validate the proposal. The extension to ultrafast charging at 1.5 C is currently in progress in our laboratory. In the latter case, several options are being considered ranging from direct paralleling of BOFs to the interleaved operation of the converters, which will require a constant switching frequency attained with pulse-width modulation (PWM). Also, the sliding-mode approach can be adapted to the PWM implementation as reported in references [36], [37].

Appendix A
Stability analysis

A. dc transformer

The small-signal dynamics of (23) at EP (Section III-D) can be described by the following set of differential equations

$$\frac{d\tilde{i_1}}{dt} = -\frac{\delta}{\beta L_2} v_{\tilde{C_1}}$$

$$\frac{dv_{\tilde{C_1}}}{dt} = \left(\frac{V_g + \frac{L_1\delta\left(V_{C_1}^* - V_B^*\right)}{L_2\beta}}{V_{C_1}^*} + \frac{\beta}{\delta} \right) \frac{\tilde{i_1}}{C_1} - \frac{I_1^* V_g}{C_1 {V_{C_1}^*}^2} \left(\frac{L_1\delta V_{C_1}^*}{L_2\beta V_g} - 1 - \frac{L_1\delta\left(V_{C_1}^* - V_B^*\right)}{L_2\beta V_g} \right) v_{\tilde{C_1}}$$

The superscript $(\sim)$ stands for a small variation around the EP. Let us define $d\tilde{i_1}/dt \triangleq y_1(\tilde{i_1}, v_{\tilde{C_1}})$ and $d\tilde{v}_{C_1}/dt \triangleq y_2(\tilde{i_1}, v_{\tilde{C_1}})$. Considering that $V_{C_1}^* = V_B^*$ and $V_g/V_{C_1}^* = I_2^*/I_1^* = -\beta/\delta$, the Jacobian matrix corresponding to above dynamics and evaluated at the EP can be expressed as follows

$$A_1 = \begin{bmatrix} \frac{\partial y_1}{\partial \tilde{i_1}}\Big|_{EP} & \frac{\partial y_2}{\partial \tilde{v}_{C_1}}\Big|_{EP} \\ \frac{\partial y_1}{\partial \tilde{i_1}}\Big|_{EP} & \frac{\partial y_2}{\partial \tilde{v}_{C_1}}\Big|_{EP} \end{bmatrix} = \begin{bmatrix} 0 & -\frac{\delta}{\beta L_2} \\ 0 & -\frac{I_1^*}{C_1 V_{C_1}^*}\left(1 + \frac{L_1\delta^2}{L_2\beta^2}\right) \end{bmatrix}$$

The characteristic equation corresponding to the previous Jacobian matrix is given by

$$s^2 + \frac{I_2^*}{C_1 V_{C_1}^*}\left(1 + \frac{L_1\delta^2}{L_2\beta^2}\right) s = 0 \tag{31}$$

In the next subsection the same approach will be used in order to obtain the characteristic equation of the G-gyrator of type II and the LFR.

B. G-gyrator of type II

The small-signal dynamics of (25) at the EP is given by:

$$\frac{d\tilde{i_2}}{dt} = -\frac{\tilde{v}_{C_1}}{L_2} \triangleq y_3(\tilde{i_2}, \tilde{v}_{C_1}) \tag{32a}$$

$$\frac{d\tilde{v}_{C_1}}{dt} = \frac{\tilde{i}_2}{C_1} - \frac{\gamma V_g}{\beta C_1 V_{C_1}^*}\tilde{v}_{C_1} \triangleq y_4(\tilde{i_2}, \tilde{v}_{C_1}) \tag{32b}$$

The corresponding Jacobian matrix at the EP is:

$$A_2 = \begin{bmatrix} \frac{\partial y_3}{\partial \tilde{i}_1}\Big|_{EP} & \frac{\partial y_4}{\partial \tilde{v}_{C_1}}\Big|_{EP} \\ \frac{\partial y_3}{\partial \tilde{i}_1}\Big|_{EP} & \frac{\partial y_4}{\partial \tilde{v}_{C_1}}\Big|_{EP} \end{bmatrix} = \begin{bmatrix} 0 & -\frac{1}{L_2} \\ \frac{1}{C_1} & -\frac{\gamma V_g}{\beta C_1 V_{C_1}^*} \end{bmatrix}$$

Consequently, the characteristic equation becomes:

$$s^2 - \frac{\gamma V_g}{\beta C_1 V_{C_1}^*} s + \frac{1}{C_1 L_2} = 0 \tag{33}$$

C. Loss-free resistor

The small-signal dynamics of (27) at the EP is as follows:

$$\frac{d\tilde{i_2}}{dt} = -\frac{\tilde{v}_{C_1}}{L_2} \triangleq y_5(\tilde{i_2}, \tilde{v}_{C_1}) \tag{34a}$$

$$\frac{d\tilde{v}_{C_1}}{dt} = \frac{1}{C_1} - \frac{\alpha V_g^2}{\beta C_1 {V_{C_1}^*}^2} \tilde{v}_{C_1} \triangleq y_6(\tilde{i_2}, \tilde{v}_{C_1}) \tag{34b}$$

The Jacobian matrix corresponding to (34) is

$$A_3 = \begin{bmatrix} \frac{\partial y_5}{\partial \tilde{i}_1}\Big|_{EP} & \frac{\partial y_6}{\partial \tilde{v}_{C_1}}\Big|_{EP} \\ \frac{\partial y_5}{\partial \tilde{i}_1}\Big|_{EP} & \frac{\partial y_6}{\partial \tilde{v}_{C_1}}\Big|_{EP} \end{bmatrix} = \begin{bmatrix} 0 & -\frac{1}{L_2} \\ \frac{1}{C_1} & -\frac{\alpha V_g^2}{\beta C_1 {V_{C_1}^*}^2} \end{bmatrix}$$

The correspnding characteristic equation is given by:

$$s^2 - \frac{\alpha V_g^2}{\beta C_1 {V_{C_1}^*}^2} s + \frac{1}{C_1 L_2} = 0 \tag{35}$$

REFERENCES

[1] G. Tamai, "What are the hurdles to full vehicle electrification? [technology leaders]," *IEEE Electrification Magazine*, vol. 7, no. 1, pp. 5–11, March 2019.

[2] S. Srdic and S. Lukic, "Toward extreme fast charging: Challenges and opportunities in directly connecting to medium-voltage line," *IEEE Electrification Magazine*, vol. 7, no. 1, pp. 22–31, March 2019.

[3] J. Jiang and C. Zhang, *Fundamentals and Applications of Lithium-ion Batteries in Electric Drive Vehicles*. John Wiley & Sons, Ltd, 2015, pp. 1–280.

[4] A. Tomaszewska, Z. Chu, X. Feng, S. O'Kane, X. Liu, J. Chen, C. Ji, E. Endler, R. Li, L. Liu, Y. Li, S. Zheng, S. Vetterlein, M. Gao, J. Du, M. Parkes, M. Ouyang, M. Marinescu, G. Offer, and B. Wu, "Lithium-ion battery fast charging: A review," *eTransportation*, vol. 1, p. 100011, 2019.

[5] C. Y. Wang, T. Liu, X. G. Yang, S. Ge, N. V. Stanley, E. S. Rountree, Y. Leng, and B. D. McCarthy, "Fast charging of energy-dense lithium-ion batteries," *Nature*, vol. 611, pp. 485–490, Oct. 2022.

[6] C. Chen, Z. Wei, and A. C. Knoll, "Charging optimization for li-ion battery in electric vehicles: A review," *IEEE Transactions on Transportation Electrification*, vol. 8, no. 3, pp. 3068–3089, Sep. 2022.

[7] Z. Guo, B. Y. Liaw, X. Qiu, L. Gao, and C. Zhang, "Optimal charging method for lithium ion batteries using a universal voltage protocol accommodating aging," *Journal of Power Sources*, vol. 274, pp. 957–964, 2015.

[8] Y. Gao, X. Zhang, Q. Cheng, B. Guo, and J. Yang, "Classification and review of the charging strategies for commercial lithium-ion batteries," *IEEE Access*, vol. 7, pp. 43 511–43 524, 2019.

[9] L. Jiang, Y. Li, Y. Huang, J. Yu, X. Qiao, Y. Wang, C. Huang, and Y. Cao, "Optimization of multi-stage constant current charging pattern based on taguchi method for li-ion battery," *Applied Energy*, vol. 259, p. 114148, 2020.

[10] M. Ye, H. Gong, R. Xiong, and H. Mu, "Research on the battery charging strategy with charging and temperature rising control awareness," *IEEE Access*, vol. 6, pp. 64 193–64 201, 2018.

[11] Y. Li, K. Li, Y. Xie, J. Liu, C. Fu, and B. Liu, "Optimized charging of lithium-ion battery for electric vehicles: Adaptive multistage constant current–constant voltage charging strategy," *Renewable Energy*, vol. 146, pp. 2688–2699, 2020.

[12] S. U. Jeon, J.-W. Park, B.-K. Kang, and H.-J. Lee, "Study on battery charging strategy of electric vehicles considering battery capacity," *IEEE Access*, vol. 9, pp. 89 757–89 767, 2021.

[13] G.-J. Chen and W.-H. Chung, "Evaluation of charging methods for lithium-ion batteries," *Electronics*, vol. 12, no. 19, 2023.

[14] J. R. González-Jiménez, F. Jiménez-Romero, Álvaro Bonilla, M. López-Luna, F. Lara-Raya, and Álvaro Caballero, "Improved electrochemical performance of fast-charging li-s batteries with constant power transfer protocol," *Journal of Energy Storage*, vol. 86, p. 111317, 2024.

[15] M. Brenna, F. Foiadelli, C. Leone, and M. Longo, "Electric vehicles charging technology review and optimal size estimation," *Journal of Electrical Engineering and Technology*, vol. 15, pp. 2539–2552, Oct. 2020.

[16] O. Lopez-Santos, D. Zambrano-Prada, L. Martinez-Salamero, A. E. Aroudi, and L. Vazquez-Seisdedos, "Unidirectional dc-dc converters for ultrafast charging of electric vehicles," in *2023 IEEE International Conference on Electrical Systems for Aircraft, Railway, Ship Propulsion and Road Vehicles & International Transportation Electrification Conference (ESARS-ITEC)*, March 2023, pp. 1–6.

[17] N. Poon, B. Pong, and C. Tse, "A constant-power battery charger with inherent soft switching and power factor correction," *IEEE Transactions on Power Electronics*, vol. 18, no. 6, pp. 1262–1269, Nov 2003.

[18] Q. Shi, S. He, H. Wang, V. Stojanovic, K. Shi, and W. Lv, "Extended state observer based fractional order sliding mode control for steer-by-wire systems," *IET Control Theory & Applications*, vol. 00, pp. 1–9, 2023.

[19] H. Wan, X. Luan, V. Stojanovic, and F. Liu, "Self-triggered finite-time control for discrete-time markov jump systems," *Information Sciences*, vol. 634, pp. 101–121, 2023.

[20] Q. Zhang, X. Song, S. Song, and V. Stojanovic, "Finite-time sliding mode control for singularly perturbed pde systems," *Journal of the Franklin Institute*, vol. 360, no. 2, pp. 841–861, 2023.

[21] S. Singer, "The application of loss-free resistors in power processing circuits," *IEEE Transactions on Power Electronics*, vol. 6, no. 4, pp. 595–600, Oct 1991.

[22] A. Cid-Pastor, L. Martinez-Salamero, A. El Aroudi, R. Giral, J. Calvente, and R. Leyva, "Synthesis of loss-free resistors based on sliding-mode control and its applications in power processing," *Control Engineering Practice*, vol. 21, no. 5, pp. 689–699, May 2013.

[23] F. Flores-Bahamonde, H. Valderrama-Blavi, L. Martínez-Salamero, J. Maixé-Altés, and G. García, "Control of a three-phase ac/dc vienna converter based on the sliding mode loss-free resistor approach," *IET Power Electronics*, vol. 7, pp. 1073–1082, May 2014.

[24] N. Rathore, D. Fulwani, A. K. Rathore, and A. R. Gautam, "Adaptive sliding mode based loss-free resistor for power-factor correction application," *IEEE Transactions on Industry Applications*, vol. 55, no. 4, pp. 4332–4343, July 2019.

[25] I. Barbi, "Series loss-free resistor: Analysis, realization, and applications," *IEEE Transactions on Power Electronics*, vol. 36, no. 11, pp. 12 857–12 866, Nov 2021.

[26] A. Kuperman, "Comment on "series loss-free resistor: Analysis, realization, and applications"," *IEEE Transactions on Power Electronics*, vol. 38, no. 3, pp. 3414–3416, March 2023.

[27] S. Cuk and R. D. Middlebrook, "Advances in switched-mode power conversion part i," *IEEE Transactions on Industrial Electronics*, vol. IE-30, no. 1, pp. 10–19, Feb 1983.

[28] S. Singer, "Gyrators application in power processing circuits," *IEEE Transactions on Industrial Electronics*, vol. IE-34, no. 3, pp. 313–318, Aug. 1987.

[29] S. Singer and R. Erickson, "Canonical modeling of power processing circuits based on the popi concept," *IEEE Transactions on Power Electronics*, vol. 7, no. 1, pp. 37–43, Jan. 1992.

[30] O. López-Santos, D. A. Zambrano-Prada, H. Valderrama-Blavi, A. Cid-Pastor, L. Vázquez-Seisdedos, A. E. Aroudi, and L. Martínez-Salamero, "Design of loss-free resistors terminated at a generic nonlinear static load," *IEEE Transactions on Circuits and Systems I: Regular Papers*, vol. 70, no. 12, pp. 5496–5506, Dec. 2023.

[31] L. Martinez-Salamero, H. Valderrama-Blavi, R. Giral, C. Alonso, B. Estibals, and A. Cid-Pastor, "Self-oscillating dc-to-dc switching converters

with transformer characteristics," *IEEE Transactions on Aerospace and Electronic Systems*, vol. 41, no. 2, pp. 710–716, April 2005.
[32] A. Cid-Pastor, L. Martinez-Salamero, C. Alonso, B. Estibals, J. Alzieu, G. Schweitz, and D. Shmilovitz, "Analysis and design of power gyrators in sliding-mode operation," *IEE Proceedings: Electric Power Applications*, vol. 152, pp. 821–826, July 2005.
[33] A. Cid-Pastor, L. Martinez-Salamero, C. Alonso, G. Schweitz, J. Calvente, and S. Singer, "Classification and synthesis of power gyrators," *IEE Proceedings: Electric Power Applications*, vol. 153, pp. 802–808, Nov. 2006.
[34] J. G. J. Shi V. Utkin, *Sliding Modes in Electromechanical Systems*, 2nd ed. London, U.K.: Taylor and Francis, 2009.
[35] S. Ozeri, D. Shmilovitz, S. Singer, and L. Martinez-Salamero, "The mathematical foundation of distributed interleaved systems," *IEEE Transactions on Circuits and Systems I: Regular Papers*, vol. 54, no. 3, pp. 610–619, March 2007.
[36] S. H. Chincholkar, W. Jiang, and C.-Y. Chan, "An improved pwm-based sliding-mode controller for a dc–dc cascade boost converter," *IEEE Transactions on Circuits and Systems II: Express Briefs*, vol. 65, no. 11, pp. 1639–1643, Nov 2018.
[37] S.-C. Tan, Y. M. Lai, and C. K. Tse, "General design issues of sliding-mode controllers in dc–dc converters," *IEEE Transactions on Industrial Electronics*, vol. 55, no. 3, pp. 1160–1174, March 2008.

David A. Zambrano-Prada received both the Electronical Engineering and Master in Control Engineering degrees in 2014 and 2019 respectively from Universidad de Ibagué, Colombia; and the PhD. degree in 2023 at Universitat Rovira i Virgili, Spain. During the period 2015 to 2019, he worked as a young researcher in the D+TEC research group of the Universidad de Ibagué in control of dc-dc converters, energy storage systems and microgrids. In 2020, he joined the Automatic Control and Industrial Electronics Research Group (GAEI) of Universitat Rovira i Virgili, where he is currently a postdoc researcher. His main research interests include control of energy storage systems within dc microgrids, electric vehicles, dc-dc converters and sliding mode control.

Abdelali El Aroudi (Senior Member, IEEE) received the bachelor's degree in physical science from the Faculté des Sciences, Université Abdelmalek Essaadi, Tetouan, Morocco, in 1995, and the Ph.D. degree (Hons.) in applied physical science from the Universitat Politècnica de Catalunya, Barcelona, Spain, in 2000. Currently, he is a Full Professor in the Department of Electronics, Electrical Engineering and Automatic Control, University Rovira o Virgili, Tarragona, Spain. His research interests are in the field of dynamics and control of power conditioning systems, power factor correction and renewable energy applications. He was an Associate Editor of the IET Circuits, Systems and Devices, Associate Editor of the IET Power Electronics and Associate Editor of the IET Electronics Letters. He also was a Guest Editor of the IEEE Journal on Emerging and Selected Topics on Circuits and Systems, in 2015, a Guest Editor of the IEEE Transactions on Circuits and Systems—II, in 2018, and Energies, from 2018 to 2023. He currently serves as an Associate Editor for International Journal of Circuit Theory and Applications, and topic editor in Energies.

Oswaldo López-Santos (Senior Member, IEEE) received the electronics engineer degree from the Universidad Distrital Francisco José de Caldas in Bogotá - Colombia in 2002, the master degree on industrial automation from the Universidad Nacional de Colombia, Bogotá - Colombia in 2011, and the PhD degree from the Institute National des Sciencies Apliquées (INSA) de Toulouse in 2015 developing his research project at LAAS-CNRS. From 2004 to 2008, he worked in Colombia as design engineer for manufacture of industrial power converters. From 2009 to 2021, he was an Associate Professor with the Electronics Engineering Department and Leader of the Research Group D+Tec (Technological Development) in the Universidad de Ibagué, Colombia. In 2020, he served at the same University as the Director of the Research Office. Currently, he is a postdoctoral researcher associated to the Research Group GAEI at the Universitat Rovira i Virgili, Tarragona, Spain. His current research interest is focused on the control of power electronic converters involved in applications such as microgrids and electric vehicles.

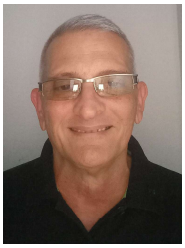

Luis Vázquez-Seisdedos received a B.S. degree in Automatic Control Engineering, a M.S. degree in Automation, and a PhD degree in Technical Science (Automation), from the Universidad de Oriente, Santiago de Cuba, Cuba, in 1982, 1999, and 2015 respectively. He has received an equivalent Ph.D. degree in Nanosystems Technologies, Bioengineering and Energy from the Rovira i Virgili University, Spain in 2022. His research interests are focused on the control of electromechanical energy conversion systems. Namely, power plants based on both fossil fuel sources and renewable energy resources (RES), electric vehicles (EV), energy storage subsystems and its hybridization, electric drives, electrical traction systems, and RES´s and EV´s integration into electrical power systems. He is currently working on ultra-fast charging of electric vehicles and intelligent active damping in microgrids and electric vehicles. Since 2009, he is a member of the TC 6.3. Power and Energy Systems Committee of IFAC.

Luis Martínez-Salamero received the Ingeniero de Telecomunicacion degree in 1978 and the Ph.D. degree in 1984, both from Universidad Politecnica de Cataluna, Barcelona, Spain. He was given the Doctor Honoris Causa degree in 2024 from Université Toulouse III Paul Sabatier, France. From 1978 to 1992, he taught circuit theory, analog electronics and power processing at the Escuela Tecnica Superior de Ingenieros de Telecomunicacion, Barcelona, Spain. From 1992 to 1993, he was a visiting professor at the Center for Solid State Power Conditioning and Control, Department of Electrical Engineering, Duke University, Durham, NC. From 2003 to 2004, 2010 to 2011, and March-September 2018 he was a visiting scholar at the Laboratory of Architecture and Systems Analysis (LAAS), National Agency for Scientific Research (CNRS), Toulouse, France. Since 1995 he has been a full professor with the Department of Electrical Electronic and Automatic Control Engineering, School of Electrical and Computer Engineering, Rovira i Virgili University, Tarragona, Spain, where he managed the Research Group in Automatic Control and Industrial Electronics (GAEI) in the period 1998-2018. His research interests include structure and control of power conditioning systems, namely, electrical architecture of satellites and electric vehicles, as well as nonlinear control of converters and drives, and power conditioning for renewable energy.